Fast, Self-Driven, Air-Stable and Broadband Photodetector Based on Vertically Aligned $PtSe_2$/GaAs Heterojunction

Long-Hui Zeng,[a] Sheng-Huang Lin,[a] Zhong-Jun Li,[b] Zhi-Xiang Zhang, [b] Teng-Fei Zhang,[b] Chao Xie, [b] Chun-Hin Mak, [a] Yang Chai, [a] Shu Ping Lau, [a] Lin-Bao Luo,*[b] Yuen Hong Tsang*[a]

[a] Department of Applied Physics and Materials Research Center, The Hong Kong Polytechnic University, Hung Hom, Kowloon, Hong Kong, 99077, China

[b] School of Electronic Science and Applied Physics, Hefei University of Technology, Hefei, Anhui 230009, China

KEYWORDS: transitional metal dichalcogenides, broadband, heterojunction, photodetector, density function theory.

ABSTRACT: Group-10 layered transitional metal dichalcogenides including PtS_2, $PtSe_2$ and $PtTe_2$ are excellent potential candidates for optoelectronic devices due to their unique properties such as high carrier mobility, tunable bandgap, stability and flexibility. Large-area platinum diselenide ($PtSe_2$) with semiconducting characteristics is far scarcely investigated. Here, we report on the development of a high performance photodetector based on vertically aligned $PtSe_2$-GaAs heterojunction which exhibited a broadband sensitivity from deep ultraviolet (DUV) to near infrared (NIR) light, with peak sensitivity from 650 to 810 nm. The I_{light}/I_{dark} ratio and responsivity of photodetector were 3×10^4 and 262 mA W^{-1} measured at 808 nm under zero bias voltage. The response speed of τ_r/τ_f were 5.5/6.5 μs, which represented the best result achieved for Group-10 TMDs based optoelectronic device thus far. According to first-principle density functional theory, the broad photoresponse ranging from visible to near infrared region is associated with the semiconducting characteristics of $PtSe_2$ which has interstitial Se atoms within the $PtSe_2$ layers. It was also revealed that the $PtSe_2$/GaAs photodetector did not exhibit performance degradation after 6 weeks in air. The generality of the above good results suggests that the vertically aligned $PtSe_2$ is an ideal material for high-performance optoelectronic systems in the future.

INTRODUCTION:

The layered two-dimensional transition disulfides (2D TMDs) with common formula of MX_2 (The M denotes a transition metal and X is a chalcogen atom, with strong in-plane covalent bonding and anisotropic layer structure with weak van der Waals bonding between layers), have attracted great attention in the past decade due to their distinctive material properties, e.g. tunable open bandgap, high carrier mobility, strong nonlinear optical properties,[1-5] which may potentially bring the revolutionary changes in diverse fields including electronics, photonics,[6, 7] catalysis,[8] laser,[9] renewable energy [10] and so on. As a new Group-10 TMDs based materials, $PtSe_2$ has come under spotlight for its tunable bandgap transition from monolayer (1.2 eV) to semimetal at bulk with zero bandgap. To date, a number of synthetic strategies have been developed for the fabrication of $PtSe_2$ layer. For instance, $PtSe_2$ flakes can be mechanically exfoliated from bulk $PtSe_2$ crystal but with very small and uncontrollable sample size.[11] To obtain larger size sample, Wang *et al* for the first time grew monolayer $PtSe_2$ film through molecular beam epitaxy-assisted selenization process.[12] Recently, the efforts of synthesizing polycrystalline $PtSe_2$ film by either chemical reaction or thermally assisted conversion (TAC) at low temperature has been reported.[13-15] The $PtSe_2$ films derived by the above method are horizontally aligned. It has been experimentally observed that $PtSe_2$ exhibits very good stability in air (>1 year). [11, 12] In addition, high mobility of $PtSe_2$ has been predicted among the highest in TMDCs, which is comparable to that of black phosphorus.[11] Because of these appealing properties, $PtSe_2$ has shown potentially important applications in various nano-devices, such as field-effect transistors,[16] and photocatalyst.[17] What is more, for the first time, a Si-$PtSe_2$ hybrid structure by combining vertically stacked $PtSe_2$ thin film with Si was fabricated, which can act as a sensitive gas sensor with extremely short response.[13] It was also found that like traditional metal-semiconductor (M-S) photodiode, the as-fabricated $PtSe_2$-Si structure exhibited pronounced photovoltaic characteristics, and was highly sensitive to 920 nm laser illuminations with very high responsivity.

Near infrared (NIR) light photodetector is vitally important for both military and civil applications including optical telecommunication, target imaging, remote version, time surveillance and environmental monitoring.[18, 19] Nowadays, the commercial IR photodetectors

are dominated by narrow-gap semiconductors such as PbS, PbSe, PbTe , HgTe and HgCdTe.[20, 21] These materials normally entail the usage of sophisticated fabrication facility. [21-23] Silicon based NIR photodetectors are also emerging recently. However, the fabrication of silicon NIR photodetectors is usually characterized by growth of narrow-gap Ge, GeSi, and HgCdTe thin film on Si using molecular beam epitaxy (MBE). Even though the above devices have high sensitivity, it is undeniable that the fabrication process is time consuming. What is more, the fabrication cost is relatively high.[24, 25] Considering the relatively small bandgap, $PtSe_2$ may find possible application in NIR detection.

In this work, we report on the synthesis of vertically aligned $PtSe_2$ multi-layer film with semiconducting characteristics for high-performance photodetector application. The $PtSe_2$ films were synthesized by a simple selenization method, which has the obvious advantages in terms of low cost, large size and well controlled overall film thickness, in comparison with conventional chemical vapor deposition (CVD) method and mechanical exfoliation.[26] Based on the vertically aligned $PtSe_2$ multi-layer film, we assembled a $PtSe_2$-GaAs heterojunction which exhibited a broadband sensitivity to illumination ranging from deep ultraviolet (DUV) to near infrared (NIR) light. Optoelectronic analysis revealed that the I_{on}/I_{off} ratio, responsivity, specific detectivity and response speed of photodetector were 3×10^4, 262 mA W^{-1}, 2.52×10^{12} Jones and 5.5/6.5 μs, respectively, which were comparable to or better than those of other TMDs photodetectors. Moreover, the present $PtSe_2$/GaAs heterojunction showed obvious sensitivity in the range of visible-near infrared, which was probably associated with the interstitial Se atoms, according to our DFT theoretical simulation. This study suggests that the present vertically aligned $PtSe_2$ film is a good candidate for assembling high-performance optoelectronic devices.

RESULTS AND DISCUSSION

The scheme in Figure 1a illustrates the procedures to fabricate the $PtSe_2$/GaAs heterojunction photodetector. The as-prepared $PtSe_2$ film was transferred onto the n-GaAs with a predefined window. An Ag paste was used as the top contact to $PtSe_2$, whereas 50 nm Au served as the back contact to n-GaAs. In this study, the $PtSe_2$ was fabricated by a simple selenization of Pt thin film on a SiO_2/Si wafer (Figure S1). From the photograph shown in Figure 1b, it can be clearly seen that the color of Si/SiO_2 wafer changes slightly from navy to slate gray, when the Pt

was transformed to $PtSe_2$. Figure 1c displays an AFM image of the $PtSe_2$ film, in which a height profile along with the marked line is given in the inset diagram and the thickness of $PtSe_2$ is approximately 35 nm. With the availability of large area $PtSe_2$ nanofilm, we are able to study the Raman spectrum of $PtSe_2$. As revealed in Figure 1d, the peak centered at 177 cm^{-1} can be assigned to the E_g in-plane vibrational mode of Se atoms and the peak centered at 206 cm^{-1} to the A_{1g} out-of-plane vibration mode.[27] Further XRD pattern in Figure 1e is characterized by three diffraction peaks located at 17.14°, 44.28° and 53.86° due to the (001), (102) and (003) crystal planes of $PtSe_2$. According to the XPS analysis, there are two peaks at 73.55 and 76.85 eV that are related to Pt $4f_{7/2}$ and Pt $4f_{5/2}$ orbitals, respectively, whereas the binding energies for the Se $3d_{5/2}$ and Se $3d_{3/2}$ are located at 54.85 and 55.65 eV.[16]

By studying the morphology using field emission scanning electron microscopy (FESEM), it can be easily found that the as-synthesized film is continuous and uniform in Figure 2a. The magnified three-dimensional AFM surface topography was shown in the right panel of Figure 2a, indicating the $PtSe_2$ film has a relatively smooth surface. The atomic ratio of Se/Pt inspected by energy-dispersive X-ray (EDS) spectroscopy was determined to be 2.11/1 (inset of Figure 2b), which is slightly higher than the stoichiometric composition of $PtSe_2$. Figure 2c-d shows the TEM images of the $PtSe_2$ layer at different magnifications, revealing that the $PtSe_2$ is polycrystalline with a vertically aligned layered structure. This special structure of $PtSe_2$ was different from the result of Ref. 13, in which vertically stacked $PtSe_2$ was obtained.[13] Understandably, such a difference is related to the usage of Pt thin film precursors with different thickness (0.5 nm Vs 12 nm). According to previous study, such a difference in Pt thickness means different density, compactness and roughness of Pt, which therefore leads to $PtSe_2$ with different alignment during selenization process. [28, 29] The detailed reason for the formation of vertically aligned $PtSe_2$ is complicated and needs further investigation. The thickness of the $PtSe_2$ film is estimated to be 35 nm, according to cross-sectional TEM image as shown in the inset of Figure 2d. Further diffraction rings from inside to outside can be readily ascribed to the (001), (100), (101), (110), (200) and (212) planes of $PtSe_2$. [30] It should be noted that, the interlayer distance of the vertically grown $PtSe_2$ has a wide distribution from 0.44 nm to 0.64 nm, with an average value of 0.58 nm. Such an interlayer distance is relatively larger than previously reported

value (~0.52 nm).[17] Considering the excessive amount of Se atoms in the $PtSe_2$ (Pt/Se=1/2.11) measured by EDS, it can be easily concluded that such an increase in interlayer distance is due to the interstitial Se atoms, which are normally located at gap between the interlayers. In addition, according to scanning transmission electron microscope (STEM) image and EDS elemental mapping analysis, both Pt and Se are homogeneously distributed over the whole film in Figure S2.

The as-fabricated $PtSe_2$/GaAs heterojunction exhibits a typical rectifying behavior without light illumination, as indicated by the dark curve in Figure 3a. In light of the good contact of both Ag/$PtSe_2$ and Au/GaAs (Figure S3, Supporting Information), the above nonlinear *I-V* characteristics stems from heterojunction formed at $PtSe_2$/GaAs contact. The rectification ratio is determined to be ~ 120 at ± 2 V, which is higher than previously studied graphene/GaAs Schottky junction (~ 24, ~ 49, ~ 100). [18, 31, 32] Figure 3b shows the photoresponse characteristics when the incident light (808 nm, 44.2 mW/cm^2) was switched on and off repeatedly. Clearly, the current of heterojunction significantly increases with light irradiation on, giving stable and repeatable I_{on}/I_{off} of 3×10^4. It is also revealed that the fabricated device can be reversibly switched quickly between low and high current states with steep rise and fall edges, indicating that electron-hole pairs could be effectively generated and separated in the $PtSe_2$/GaAs heterojunction. In fact, the photocurrent of the device is highly dependent on the light intensity. Figure 3c plots the *I-V* curves under the light intensities ranging from 0.52 to 38.5 mW/cm^2. Apparently, with the increase of light intensity, the photocurrent is observed to increase gradually. So, it is easily noted that the device exhibits pronounced photovoltaic behaviors under light illumination within the measurement range from -0.4 to +0.4 V, indicating the $PtSe_2$/GaAs heterojunction can function as a self-driven photodetector.[33] Further photoresponse characteristic in Figure 3d shows that the $PtSe_2$/GaAs device can be switched between on and off states under varied light intensity with good reproducibility.

To evaluate the device performance of the current $PtSe_2$/GaAs photodetector, the responsivity (*R*), specific detectivity (D^*) and response speed were then calculated. *R* is defined as the photocurrent generated per unit power of the incident light on the effective area and was

obtained from the experimental data by using the formula：

$$R(AW^{-1}) = \frac{I_p - I_d}{P_{opt} S} \quad (1)$$

where I_p is the photocurrent, I_d the dark current, P_{opt} the incident-light intensity, S the effective illuminated area (S = 0.04 cm^2). On the other hand, the D^* represents the ability of a detector to detect weak optical signals, which can be calculated from the following equation:

$$D^* = A^{1/2} R / (2qI_d)^{1/2} \quad (2)$$

where A is the effective area of device (A = 0.09 cm^2), q the electronic charge and R the responsivity respectively. Based on Equation (1) and (2), R and D^* of $PtSe_2$/GaAs heterojunction were estimated to be 262 mAW^{-1} and 2.52×10^{12} Jones under light intensity of 0.11 mW/cm^2 at zero bias voltage, respectively. Figure 3e plots both R and D^* under illumination of various light intensities. It is noted that both R and D^* of photodetector reduced with increasing light intensity. This finding is understandable as the photo-generated electrons can be captured by the trap states under lower light intensity, therefore leading to a reduce in recombination possibility.[34], [35] In addition, the photocurrent current as a function of the light intensity is shown in Figure 3f and the curve was fitted to obtain law of $J_s \propto P^{0.83}$. The nonunity exponent of the law is due to the complex process of electron-hole generation, trapping and recombination activity within the $PtSe_2$/GaAs heterojunction.[36]

Next, the wavelength-dependent responsivity and specific detectivity of the $PtSe_2$/GaAs device were studied. Figure 4a shows the continuous spectral responsivity in the range from 200-1200 nm. Obviously, this device exhibits broad photoresponse, with peak response in the range from 650 to 810 nm. Such peak response can be exclusively attributed to the contribution from $PtSe_2$ layer, when compared with the spectral responsivity of $PtSe_2$, GaAs and Pt/GaAs devices, shown in Figure S4. In Figure S4a, the pure $PtSe_2$ exhibits a high responsivity from 500-810 nm and the responsivity values decrease when the incident light wavelength outside this wavelength region. Due to the limited light absorption arising from the small thickness, the absolute responsivity value of the pure $PtSe_2$ is much lower than that of $PtSe_2$/GaAs. On the other hand, for $PtSe_2$/GaAs device, the photocurrent is mainly contributed by the generation of photocarriers in GaAs, which could be confirmed by the much higher responsivity value and the

sharply decreased responsivity at ~810 nm similar to that of pure GaAs and Pt/GaAs devices (Figure S4b and c). In addition, due to the relatively strong light absorption of $PtSe_2$ from 500-810 nm, photocarriers generated in $PtSe_2$ also contribute to the photocurrent, which eventually gives a high responsivity from 500-810 nm with peak values from 650-810 nm. The maximum R and D^* values are ~ 0.262 A/W and 2.52 $\times 10^{12}$ Jones, which are comparable to the reported values for graphene-based photodetector (R~1.73 mA/W, D^*~1.83×10^{11} Jones),[18] MoS_2/GaAs (R~0.43 mA/W, D^*~2.28×10^{11} Jones),[37] and multilayer MoS_2 phototransistor (R~120 mA/W, D^*~10^{10} Jones).[38] As we will discuss later, this abnormal spectral selectivity is associated with the semiconducting characteristics of $PtSe_2$ layer. It is worth noting that even though the responsivity is relatively low in deep UV and near infrared range, the present $PtSe_2$ films based device is still able to detect both deep UV and near infrared light illumination. As shown in Figure 4c-d, the $PtSe_2$/GaAs device can be readily switched between low-/high-conduction states, when the illumination with repeated turn on and off. The excellent reproducibility suggests that this device may also find application for broadband photodetectors.[39]

It is known that GaAs based photodetectors usually exhibit the strongest sensitivity at around 850 nm, [18, 40] due to the band gap of 1.42 eV. This is quite different from the present GaAs/$PtSe_2$ device with peak photoresponse in the range from 650 to 810 nm. Such a difference in spectral selectivity is without question attributed to the $PtSe_2$. To unveil the authentic origin behind this phenomenon, we then studied the electronic band of various structures by first-principle density functional theory (DFT) calculation. The geometrical and band structures of the $PtSe_2$ thin films with 1-, 2-, and 3-layer are presented in Figure 5(a-c). One can see from the figure that the $PtSe_2$ thin films with 1- and 2-layer show semiconducting characteristics, and the band gap clearly becomes smaller from 1 layer to 2 layers. As the thickness of thin films increase to 3 layers, the metallic character occurs. Therefore, following this decreasing trend of band gap, one can conclude that the present free-standing $PtSe_2$ thin films possess metallic behavior, which is consistent with previous study.[11, 41] Like graphene, this metallic behavior however cannot induce a change in spectral selectivity in that the bandgap was not opened up. So, the doping effects on electronic structures of the $PtSe_2$ thin films, Se-vacancy, Pt-vacancy, and

the interstitial incorporation of Se between two neighboring layers are then taken into account in the supercells. In view of the computational cost, the 3×3 supercell of the $PtSe_2$ thin films with 3-layer is employed in the calculation. In this supercell, the separation between the neighboring dopants is larger than 11 Å. This distance facilitates to reduce the interaction among the dopants. On the other hand, the $PtSe_2$ thin films with 3-layer has similar metallic character as the thin film with more layers. The Se-vacancy and Pt-vacancy are modeled in the topmost and bottommost layers, and the interstitial atoms of Se are incorporated between the two neighboring layers of the supercell. The band structures in Figure 5(d-f) indicate that the $PtSe_2$ thin films with the Se-vacancy and Pt-vacancy both possess metallic characters, whereas the system with the interstitial incorporation of Se is semiconducting. It is noted here that in the present work the $PtSe_2$ thin films are synthesized in the Se-rich condition. This will facilitate Se atoms to interstitially incorporate into parallel layers. In this type of doping, the atomic ratio between Se and Pt is more than 2, which are consistent with the present experimental measurements (See inset of Figure 2b). To further study the concentration influence of the interstitial incorporation of Se on electronic structures, the band structures of the 2×2 and 4×4 supercells with 3-layer are calculated and presented in Figure S5. It can be seen from the figure that the defect levels is largely determined by the doping concentration. Based on the above results, it can be easily concluded that the interstitial incorporation of Se between two layers (see Figure 2f), can lead to the opening of bandgap of $PtSe_2$, and therefore will be responsible for the shift in spectral response.[42]

To further understand the photoresponse and spectral selectivity of the photodetector under light irradiation, we correlated the response characteristic with carrier transport process and the energy band diagrams of $PtSe_2$/GaAs heterojunction structure and proposed a mechanism here based on the above results (see Figure 6a). Thus, work function of $PtSe_2$ is investigated by using ultraviolet photoemission spectroscopy (UPS) as shown in Figure S6a, indicating that Fermi level of the $PtSe_2$ is located at 5.12 eV, [43] which is higher than that of GaAs. The typical transfer of the fabricated transistor based on $PtSe_2$ films is shown in Figure S6b, indicating the *p*-type behavior of prepared $PtSe_2$ films. Due to difference in Femi level (E_F), once the *p*-type $PtSe_2$ is in contact with *n*-type GaAs, the electrons would diffuse from GaAs into $PtSe_2$ while holes should

diffuse from $PtSe_2$ in to GaAs. Therefore, the energy levels near the GaAs surface will bend upward whereas the energy levels near $PtSe_2$ surface will bend downward, eventually the Fermi levels of $PtSe_2$ and GaAs align in the same level, leading to the formation of built-in electric field near the $PtSe_2$/GaAs interface.[44] As often observed in graphene/semiconductor interface, under light irradiation, the electron-hole pairs will be generated in GaAs at the interface, and then separated by the built-in electric field as shown in Figure 6b, giving rise to generation of photocurrent. Due to the interstitial Se atoms during this photosensing process, parts of $PtSe_2$ layer will also strongly absorb incident light with wavelength of 650-810 nm, converting the photons to electron-hole pairs, and finally contribute to the photocurrent in the external circuit. Namely, the $PtSe_2$/GaAs heterojunction display the stronger sensitivity between 650 and 810 nm.

The response speed is another critical parameter of photodetectors, which reflects the ability of a photodetector to follow a varied optical signal.[39, 45] The response speed of $PtSe_2$/GaAs heterojunction was measured by using a chopped laser beam with varied frequencies to generate pulsed light. The schematic illustration of the measurement is shown in Figure 7a, in which the temporal photoresponse signal (photovoltage with time) was recorded by a digital oscilloscope under the illumination of the pulsed red diode laser with several different frequencies from 100 Hz to 50 kHz. Figure 7b-d shows that the photoresponse of the heterojunction device to pulsed light. Obviously, the response is very fast with excellent good repeatability in the frequency 1 kHz, 5 kHz, 50 kHz. From the magnified photoresponse curve in Figure 7e, the response time can be quantified. In the time domain, the speed of a photodetector is often characterized by the rise/fall time (τ_r/τ_f). The time needed for the current to increase from 10% to 90% of the peak value or vice versa is defined as the rise and fall time, respectively. [46] Our device yield a rise time (τ_r) and fall time (τ_f) of 5.5 and 6.5 μs at zero external bias voltage, respectively. However, this response speed is slightly slower than the results at - 2 V at the same frequency of 50 kHz (Optoelectronic study and test at - 2 V refer to Figure S7) due to a reduced depletion layer capacitance under reverse bias.[47] It is noted that the response speed is faster than other 2D materials based photodetectors (see Table 1).[48-53] Such a relatively fast response speed is related to the special structure, which is beneficial for the separation and transport of photo-generated electron-hole carriers. As a matter of fact, this response speed can be further optimized by

reducing the capacitance of the device or the thickness of the GaAs material. Besides, the relative balance (V_{max}-V_{min})/V_{max} of the photovoltage as a function of frequency in a range of 100 Hz ~ 50 kHz was depicted in Figure 7f. The 3-dB frequency that was defined as the frequency at which response dropped 0.707 of the initial value was estimated to be 8 kHz and the relative balance only decreases by less than 20% even at a high frequency of 50 kHz, suggesting that the $PtSe_2$/GaAs heterojunction photodetector is capable of monitoring fast optical signals.[54]

The long-term stability of photodetector remains an important concern for device application. Therefore, we investigate the air stability of $PtSe_2$/GaAs photodetector by placing sample in air for 6 weeks without any encapsulation. Remarkably, the device showed high stability, and no obvious degradation in sensitivity was observed (Figure 8a-b). The high device stability is not only directly associated with excellent air stability of $PtSe_2$ film and GaAs, but also the high quality of heterojunction based $PtSe_2$/GaAs. As illustrated in Figure 8c, the XPS spectra of the aged $PtSe_2$ sample are virtually unchanged after 6 weeks storage in air. Moreover, the Raman spectra of the pristine $PtSe_2$ and the sample after 6 weeks aging in air were shown in Figure 8d. It is clearly observed that Raman spectra of the aged sample are similar to the pristine $PtSe_2$. These results indicate the stability of $PtSe_2$ in air is much better than that of black phosphorus.[55]

CONCLUSION

In summary, we have demonstrated an air-stable, self-powered and broadband photodetector based on vertically aligned structure $PtSe_2$/GaAs heterojunction. Such a heterojunction structure has exhibited broad sensitivity to illumination ranging from DUV to NIR light, with peak sensitivity to illumination ranging from 650 to 810 nm at zero bias voltage. The I_{on}/I_{off} ratio, responsivity, specific detectivity and response speed of the studied photodetector were estimated to be 3×10^4, 262 mA W^{-1}, 2.52×10^{12} Jones and 5.5/6.5 μs, respectively, which were comparable to or better than that of other TMDs photodetectors. Further DFT theoretical simulation results revealed that the peak sensitivity in the range from 650 nm (visible) and 810 nm (near infrared) was probably related to the interstitial Se atoms in $PtSe_2$ films, which will lead to opening the bandgap. It is expected that the high-performance $PtSe_2$/GaAs heterojunction photodetector demonstrated in this paper will open up a new pathway for the development of next-generation 2D Group-10 materials based optoelectronic devices.

METHODS

Materials Synthesis and Characterization: The $PtSe_2$ in this work was grown by a simple selenization method. In brief, 12 nm Pt film was firstly deposited on SiO_2/Si (300 nm SiO_2 thickness) using magnetron sputtering system. The metal-deposited SiO_2/Si substrates were placed at the center zone of the growth furnace and elemental selenium powder (99.99% purity) were placed at the upstream side. Selenium was evaporated at 220°C dragged by 50 SCCM (Standard Cubic Centimeter per Minutes) argon flow. The center temperature of the tube furnace was set to be 420 °C. After selenization for 1 hour, a thin film gray in color, will be formed at the substrate. The absorption spectra of $PtSe_2$ on quartz glass, GaAs substrate, and $PtSe_2$/GaAs heterojunction were recorded using a Perkin Elmer Lambda 900 UV/VIS/NIR spectrometer. The Raman spectra measurements were carried out on a HORIBA Raman spectrometer with a 488 nm argon ion laser. The X-ray diffraction (XRD) pattern was recorded using a RigakuSmartLab X-ray diffractometer. The topography of samples was obtained by atomic force microscopy (AFM, VeecoNanoscope V). The morphology of the $PtSe_2$ was observed by scanning electron microscope (SEM, JEOL Model JSM-6490). The XPS measurements were performed using a monochromatic Al Kα s+-ource (1486.6 eV) produced by the XPS system. The morphology, crystal structure and chemical composition were investigated using a field emission transmission electron microscope (FETEM, JEOL Model JEM-2100F), equipped with an energy dispersive spectrometer (EDS).

Device fabrication and characterization: To fabricate the $PtSe_2$/GaAs heterojunction photodetector, a 200 nm-thick SiO_2 film was deposited on a GaAs wafer using a shadow mask to form a window (0.3 cm × 0.3 cm), in which the $PtSe_2$ film will be transferred. The $PtSe_2$ films were spin-coated with 5 wt. % polymethylmethacrylate (PMMA) in chlorobenzene, and then the underlying SiO_2/Si was removed in NaOH solution. The $PtSe_2$ film was rinsed in deionized water to remove the remaining ions. Afterwards, the above GaAs was soaked in deionized water solution, and then slowly lifted to transfer the $PtSe_2$ films on GaAs surface. Finally, a drop of Ag paste was then placed at the centers of the $PtSe_2$ films. The optoelectronic characterization of the device was performed using a semiconductor parameter analyzer system (Keithley 4200-SCS) at

room temperature. To investigate the spectral response and response speed of the heterojunction devices, a home-built optoelectronic system composed of a light source (LE-SP-LS-XE), a monochromator (LE-SP-M300), an oscilloscope (Tektronix, TDS2012B), and an optical chopper (LE-oc120) was employed.

Computational Method: All calculations are performed based on density functional theory (DFT) method implemented in the Vienna ab initio simulation package (VASP).[56-59] The exchange correlation potential is approximated by the generalized gradient approximation (GGA) with Perdew-Burke-Ernzerhof (PBE) functional.[60] To describe correctly van der Waals (vdW) interaction, the DFT-D3 method with Becke-Jonson damping is employed in the calculation.[61] Electronic wave functions are expanded using a plane-wave basis set with a cutoff energy of 350 eV. The $PtSe_2$ thin films can be cleaved from the (0001) surface of the bulk which belongs to the D_{3d}^3 ($P\bar{3}m1$) space group of the trigonal system. In the $PtSe_2$ thin films with 1-layer, one atomic layer of Pt is sandwiched between two atomic layers of Se. For the $PtSe_2$ thin films with 1-, 2-, and 3-layer, the 1×1 primitive cells are chosen and a k-point set of 40×40×1 are employed in geometrical optimization and electronic structure calculations. For the $PtSe_2$ thin films with 3-layer, the 2×2, 3×3, and 4×4 supercells are used to investigate the doping effects on the electronic structures. In geometrical and electronic structure calculations, the k-point sets of 35×35×1, 25×25×1, and 15×15×1 are employed for these three supercells, respectively. A vacuum space of 20 Å is used along the z-direction perpendicular to two dimensional planes to eliminate the interaction among the periodic images. The full-relaxation of structures is carried out until the force component on each atom is less than 0.01 eV/Å, and the convergence criterion is 10^{-5} eV for energy.

AUTHOR INFORMATION

Corresponding Authors

E-mail: luolb@hfut.edu.cn,

E-mail:Yuen.Tsang@polyu.edu.hk

Author Contributions

Longhui Zeng and Shenghuang Lin contributed equally to this work.

ACKNOWLEDGMENTS

This work was supported by the National Natural Science Foundation of China (NSFC, Nos. 61675062，61575059, 21501038), the Fundamental Research Funds for the Central Universities (2013HGCH0012, 2014HGCH0005), the China Postdoctoral Science Foundation (103471013), the Research Grants Council of Hong Kong, China (Project Number: GRF 152109/16E PolyU B-Q52T) and the Hong Kong Polytechnic University (Project number: 4-BCCW, 1-ZVGH).

REFERENCES

[1] X. Yin, Z. Ye, D. A. Chenet, Y. Ye, K. O'Brien, J. C. Hone, X. Zhang, *Science* **2014**, *344*, 488.

[2] P. Wang, S. Liu, W. Luo, H. Fang, F. Gong, N. Guo, Z. G. Chen, J. Zou, Y. Huang, X. Zhou, J. Wang, X. Chen, W. Lu, F. Xiu, W. Hu, *Adv. Mater.* **2017**, *29*, 1.

[3] M. Buscema, D. J. Groenendijk, S. I. Blanter, G. A. Steele, H. S. van der Zant, A. Castellanos-Gomez, *Nano Lett.* **2014**, *14*, 3347.

[4] C. Yan, L. Gan, X. Zhou, J. Guo, W. Huang, J. Huang, B. Jin, J. Xiong, T. Zhai, Y. Li, *Adv. Funct. Mater.* **2017**, *27*, 1702918.

[5] T. Hallam, S. Monaghan, F. Gity, L. Ansari, M. Schmidt, C. Downing, C. P. Cullen, V. Nicolosi, P. K. Hurley, G. S. Duesberg, *Appl. Phys. Lett.* **2017**, *111*, 203101.

[6] C. Xie, C. Mak, X. Tao, F. Yan, *Adv. Funct. Mater.* **2017**, *27*, 1.

[7] J. Chu, F. Wang, L. Yin, L. Lei, C. Yan, F. Wang, Y. Wen, Z. Wang, C. Jiang, L. Feng, J. Xiong, Y. Li, J. He, *Adv. Funct. Mater.* **2017**, *27*, 1701342.

[8] X. Chia, A. Adriano, P. Lazar, Z. Sofer, J. Luxa, M. Pumera, *Adv. Funct. Mater.* **2016**, *26*, 4306.

[9] M. Zhang, R. C. T. Howe, R. I. Woodward, E. J. R. Kelleher, F. Torrisi, G. Hu, S. V. Popov, J. R. Taylor, T. Hasan, *Nano Res.* **2015**, *8*, 1522.

[10] K. C. Kwon, S. Choi, K. Hong, C. W. Moon, Y.-S. Shim, D. H. Kim, T. Kim, W. Sohn, J.-M. Jeon, C.-H. Lee, K. T. Nam, S. Han, S. Y. Kim, H. W. Jang, *Energy Environ. Sci.* **2016**, *9*, 2240.

[11] Y. Zhao, J. Qiao, Z. Yu, P. Yu, K. Xu, S. P. Lau, W. Zhou, Z. Liu, X. Wang, W. Ji, Y. Chai, *Adv. Mater.* **2017**, *29*, 1.

[12] Y. Wang, L. Li, W. Yao, S. Song, J. T. Sun, J. Pan, X. Ren, C. Li, E. Okunishi, Y. Q. Wang, E. Wang, Y. Shao, Y. Y. Zhang, H. T. Yang, E. F. Schwier, H. Iwasawa, K. Shimada, M. Taniguchi, Z. Cheng, S. Zhou, S. Du, S. J. Pennycook, S. T. Pantelides, H. J. Gao, *Nano Lett.* **2015**, *15*, 4013.

[13] C. Yim, K. Lee, N. McEvoy, M. O'Brien, S. Riazimehr, N. C. Berner, C. P. Cullen, J. Kotakoski, J. C. Meyer, M. C. Lemme, *ACS Nano* **2016**, *10*, 9550.

[14] A. Ali Umar, S. K. Md Saad, M. Mat Salleh, *ACS Omega* **2017**, *2*, 3325.

[15] C. Yim, V. Passi, M. C. Lemme, G. S. Duesberg, C. Ó. Pallechi, D. Fadil, N. McEvoy, *arXiv preprint arXiv:1707.06824* **2017**.

[16] Z.G. Wang, Q. Li, F. Besenbacher, a. M. D. Dong, *Adv. Mater.* **2016**, *28*, 10224.

[17] K. Ullah, S. Ye, Z. Lei, K.-Y. Cho, W.-C. Oh, *Catal. Sci. Technol.* **2015**, *5*, 184.

[18] L.-B. Luo, J.-J. Chen, M.-Z. Wang, H. Hu, C.-Y. Wu, Q. Li, L. Wang, J.-A. Huang, F.-X. Liang, *Adv. Funct. Mater.* **2014**, *24*, 2794.

[19] L. B. Luo, L. H. Zeng, C. Xie, Y. Q. Yu, F. X. Liang, C. Y. Wu, L. Wang, J. G. Hu, *Sci. Rep.* **2014**, *4*, 3914.

[20] L. Tang, R. Ji, X. Li, G. Bai, C. P. Liu, J. Hao, J. Lin, H. Jiang, K. S. Teng, Z. Yang, S. P. Lau, *ACS Nano* **2014**, *8*, 6312.

[21] P. Norton, *Opto-Electron. Rev.* **2002**, *10*, 159.

[22] R. Sporken, S. Sivananthan, K. K. Mahavadi, G. Monfroy, M. Boukerche, J. P. Faurie, *Appl. Phys. Lett.* **1989**, *55*, 1879.

[23] L. Ye, H. Li, Z. Chen, J. Xu, *ACS Photonics* **2016**, *3*, 692.

[24] V. M. Bazovkin, S. A. Dvoretskiy, A. A. Guzev, A. P. Kovchavtsev, D. V. Marin, Z. V. Panova, I. V. Sabinina, Y. G. Sidorov, G. Y. Sidorov, A. V. Tsarenko, V. S. Varavin, V. V. Vasiliev, M. V. Yakushev, *Phys. Stat. Sol. (c)* **2016**, *13*, 651.

[25] S. Ghosh, S. M. Han, *IEEE Electron Dev. Lett.* **2014**, *35*, 900.

[26] L. Tao, H. Long, B. Zhou, S. F. Yu, S. P. Lau, Y. Chai, K. H. Fung, Y. H. Tsang, J. Yao, D. Xu, *Nanoscale* **2014**, *6*, 9713.

[27] M. O'Brien, N. McEvoy, C. Motta, J.-Y. Zheng, N. C. Berner, J. Kotakoski, K. Elibol, T. J. Pennycook, J. C. Meyer, C. Yim, M. Abid, T. Hallam, J. F. Donegan, S. Sanvito, G. S. Duesberg, *2D Mater.* **2016**, *3*, 021004.

[28] Y. Jung, J. Shen, Y. Liu, J. M. Woods, Y. Sun, J. J. Cha, *Nano Lett.* **2014**, *14*, 6842.

[29] D. Kong, H. Wang, J. J. Cha, M. Pasta, K. J. Koski, J. Yao, Y. Cui, *Nano Lett.* **2013**, *13*, 1341.

[30] W.-C. Oh, K. Ullah, L. Zhu, Z.-D. Meng, S. Ye, S. Sarkar, *Mat. Sci. Semicon. Proc.* **2014**, *25*, 34.

[31] L.-B. Luo, H. Hu, X.-H. Wang, R. Lu, Y.-F. Zou, Y.-Q. Yu, F.-X. Liang, *J. Mater. Chem. C* **2015**, *3*, 4723.

[32] W. Jie, F. Zheng, J. Hao, *Appl. Phys. Lett.* **2013**, *103*, 233111.

[33] H. Sun, T. Lei, W. Tian, F. Cao, J. Xiong, L. Li, *Small* **2017**, *13*, 1701042.

[34] G. Konstantatos, I. Howard, A. Fischer, S. Hoogland, J. Clifford, E. Klem, L. Levina, E. H. Sargent, *Nature* **2006**, *442*, 180.

[35] W. Y. Kong, G. A. Wu, K. Y. Wang, T. F. Zhang, Y. F. Zou, D. D. Wang, L. B. Luo, *Adv. Mater.* **2016**,

28, 10725.

[36] H. Kind, H. Yan, B. Messer, M. Law, P. Yang, *Adv. Mater.* **2002**, *14*, 158.

[37] Y. Zhang, Y. Yu, X. Wang, G. Tong, L. Mi, Z. Zhu, X. Geng, Y. Jiang, *J. Mater. Chem. C* **2017**, *5*, 140.

[38] W. Choi, M. Y. Cho, A. Konar, J. H. Lee, G. B. Cha, S. C. Hong, S. Kim, J. Kim, D. Jena, J. Joo, S. Kim, *Adv. Mater.* **2012**, *24*, 5832.

[39] J. Mao, Y. Yu, L. Wang, X. Zhang, Y. Wang, Z. Shao, J. Jie, *Adv. Sci.* **2016**, *3*, 1600018.

[40] D. Melisi, M. A. Nitti, M. Valentini, A. Valentini, T. Ligonzo, G. De Pascali, M. Ambrico, *Beilstein J. Nanotechnol.* **2014**, *5*, 1999.

[41] P. Li, L. Li, X. C. Zeng, *J. Mater. Chem. C* **2016**, *4*, 3106.

[42] H. B. Zhang, X. J. Zhang, C. Liu, S. T. Lee, J. S. Jie, *ACS Nano* **2016**, *10*, 5113.

[43] Y. Park, V. Choong, Y. Gao, B. R. Hsieh, C. W. Tang, *Appl. Phys. Lett.* **1996**, *68*, 2699.

[44] L. ow Wang, J. Jie, Z. Shao, Q. Zhang, X. Zhang, Y. Wang, Z. Sun, S.-T. Lee, *Adv. Funct. Mater.* **2015**, *25*, 2910.

[45] L. Zeng, C. Xie, L. Tao, H. Long, C. Tang, Y. H. Tsang, J. Jie, *Opt. Express* **2015**, *23*, 4839.

[46] B. Nie, J. G. Hu, L. B. Luo, C. Xie, L. H. Zeng, P. Lv, F. Z. Li, J. S. Jie, M. Feng, C. Y. Wu, Y. Q. Yu, S. H. Yu, *Small* **2013**, *9*, 2872.

[47] A. Osinsky, S. Gangopadhyay, R. Gaska, B. Williams, M. A. Khan, D. Kuksenkov, H. Temkin, *Appl. Phys. Lett.* **1997**, *71*, 2334.

[48] C. Lan, C. Li, S. Wang, T. He, T. Jiao, D. Wei, W. Jing, L. Li, Y. Liu, *ACS Appl. Mater. Interfaces* **2016**, *8*, 18375.

[49] Y. Zhang, Y. Yu, L. Mi, H. Wang, Z. Zhu, Q. Wu, Y. Zhang, Y. Jiang, *Small* **2016**, *12*, 1062.

[50] X. An, F. Liu, Y. J. Jung, S. Kar, *Nano Lett.* **2013**, *13*, 909.

[51] N. Perea-López, A. L. Elías, A. Berkdemir, A. Castro-Beltran, H. R. Gutiérrez, S. Feng, R. Lv, T. Hayashi, F. López-Urías, S. Ghosh, B. Muchharla, S. Talapatra, H. Terrones, M. Terrones, *Adv. Funct. Mater.* **2013**, *23*, 5511.

[52] Z. Yang, W. Jie, C. H. Mak, S. Lin, H. Lin, X. Yang, F. Yan, S. P. Lau, J. Hao, *ACS Nano* **2017**, *11*, 4225.

[53] L. H. Zeng, M. Z. Wang, H. Hu, B. Nie, Y. Q. Yu, C. Y. Wu, L. Wang, J. G. Hu, C. Xie, F. X. Liang, L. B. Luo, *ACS Appl. Mater. Interfaces* **2013**, *5*, 9362.

[54] C. Xie, B. Nie, L. Zeng, F.-X. Liang, M.-Z. Wang, L. Luo, M. Feng, Y. Yu, C.-Y. Wu, Y. Wu, *ACS*

Nano **2014**, *8*, 4015.

[55] J. D. Wood, S. A. Wells, D. Jariwala, K. S. Chen, E. Cho, V. K. Sangwan, X. Liu, L. J. Lauhon, T. J. Marks, M. C. Hersam, *Nano Lett.* **2014**, *14*, 6964.

[56] P. E. Blöchl, *Phys. Rev. B* **1994**, *50*, 17953.

[57] G. Kresse, J. Furthmüller, *Comp. Mater. Sci.* **1996**, *6*, 15.

[58] G. Kresse, D. Joubert, *Phys. Rev. B* **1999**, *59*, 1758.

[59] Z. Li, W. Xu, Y. Yu, H. Du, K. Zhen, J. Wang, L. Luo, H. Qiu, X. Yang, *J. Mater. Chem. C* **2016**, *4*, 362.

[60] J. P. Perdew, K. Burke, M. Ernzerhof, *Phys. Rev. Lett.* **1996**, *77*, 3865.

[61] S. Grimme, J. Antony, S. Ehrlich, H. Krieg, *J. Chem. Phys.* **2010**, *132*, 154104.

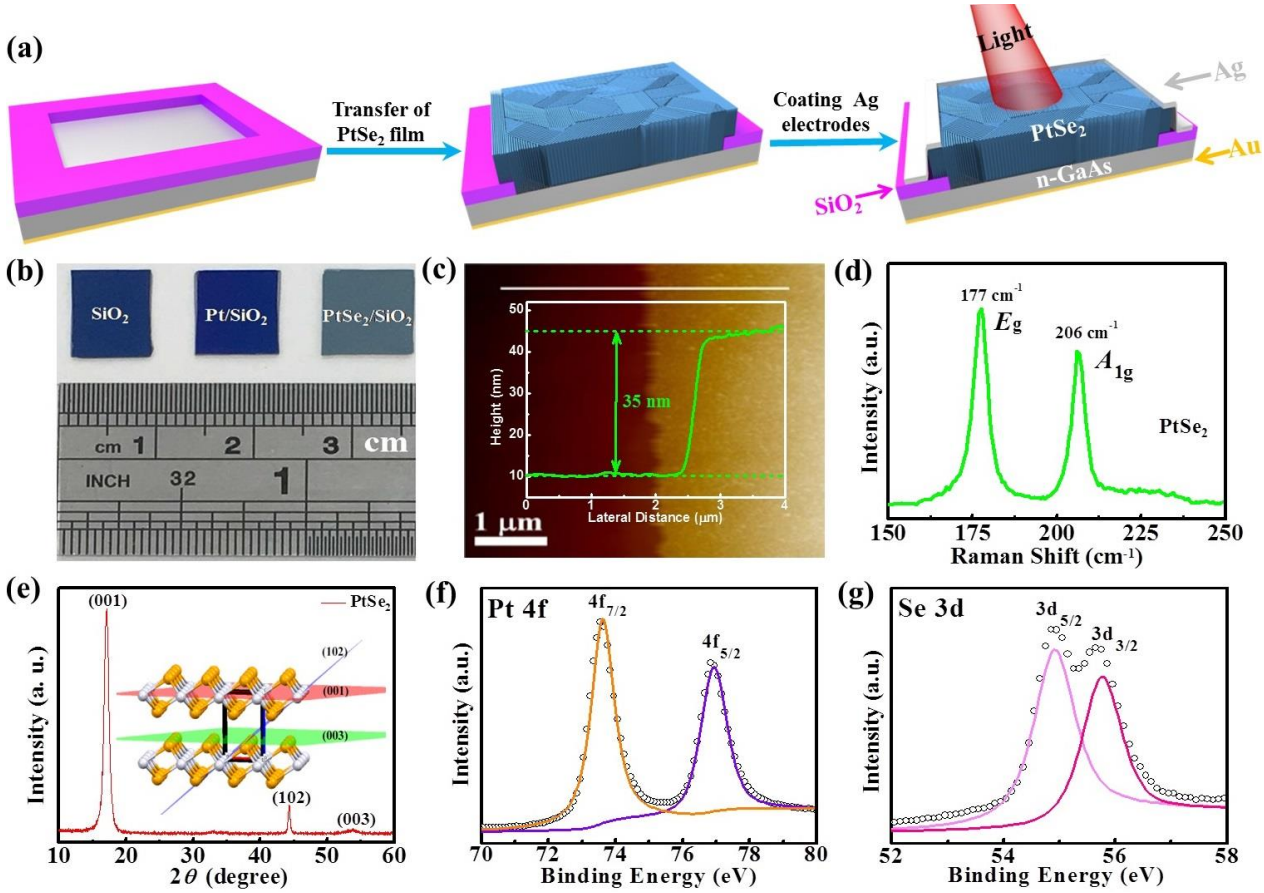

Figure 1 (a) Schematic illustration of the fabrication steps of $PtSe_2$/GaAs heterojunction based photodetector. (b) Photographs of SiO_2/Si wafer, Pt/SiO_2/Si, $PtSe_2$/SiO_2/Si. (c) AFM image of the $PtSe_2$ film on the SiO_2/Si substrate, the inset shows the height profile along the white line marked in (c). (d) Raman spectra of $PtSe_2$ nanofilm. (e) XRD pattern of $PtSe_2$ film and inset shows three-dimensional atomic structure diagram of sample. (f-g) The high resolution XPS spectra of Pt 4f and Se 3d.

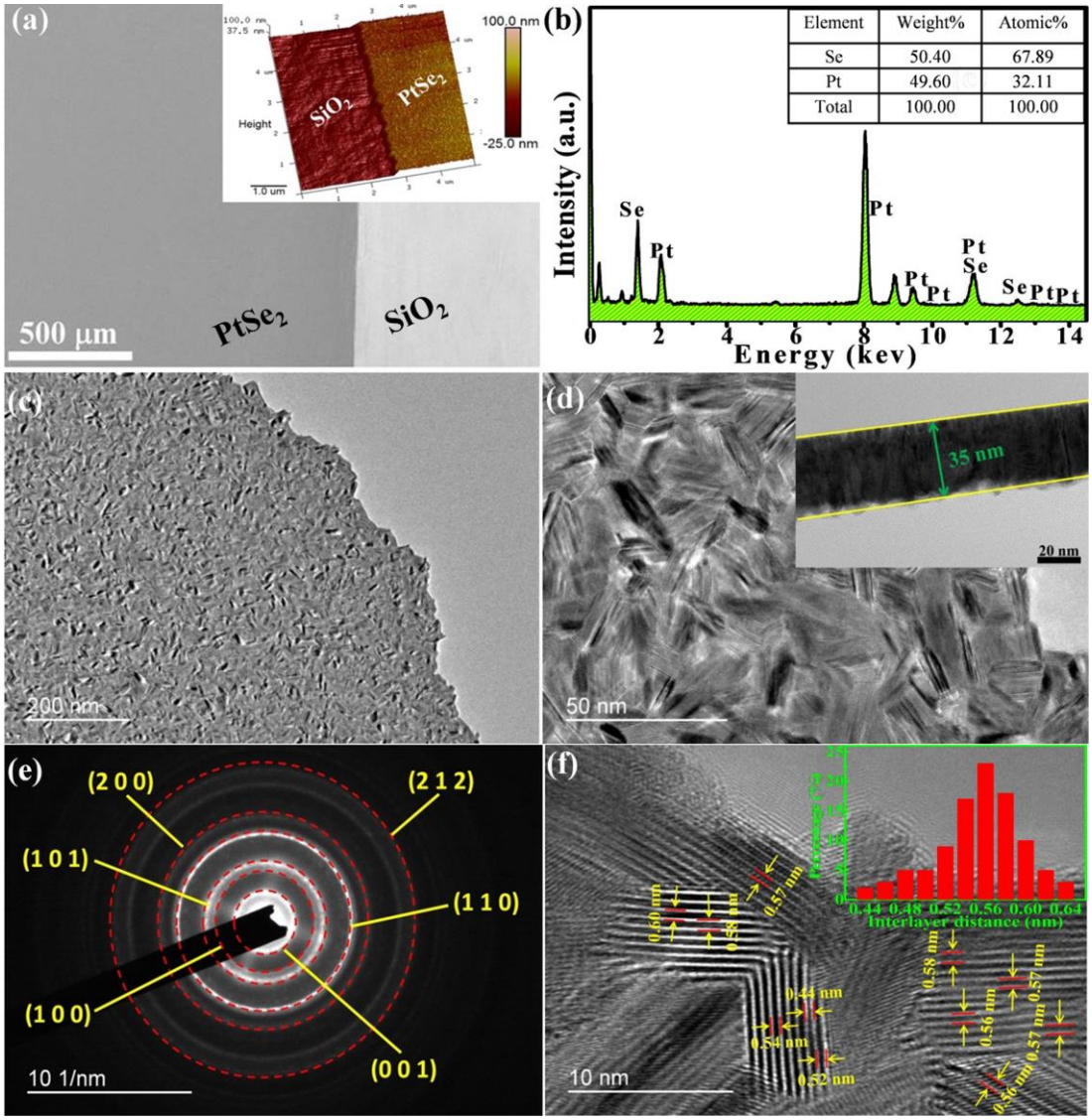

Figure 2 (a) The FESEM image of $PtSe_2$ image on a SiO_2/Si wafer, the inset shows three dimensional AFM image of $PtSe_2$. (b) The EDS spectrum of the $PtSe_2$ sample. (c-d) TEM images of synthesized $PtSe_2$ nanofilm with different magnification. (e) The SAED pattern of the $PtSe_2$ sample. (f) HRTEM image of the $PtSe_2$, the inset shows statistical distribution of interlayer distance.

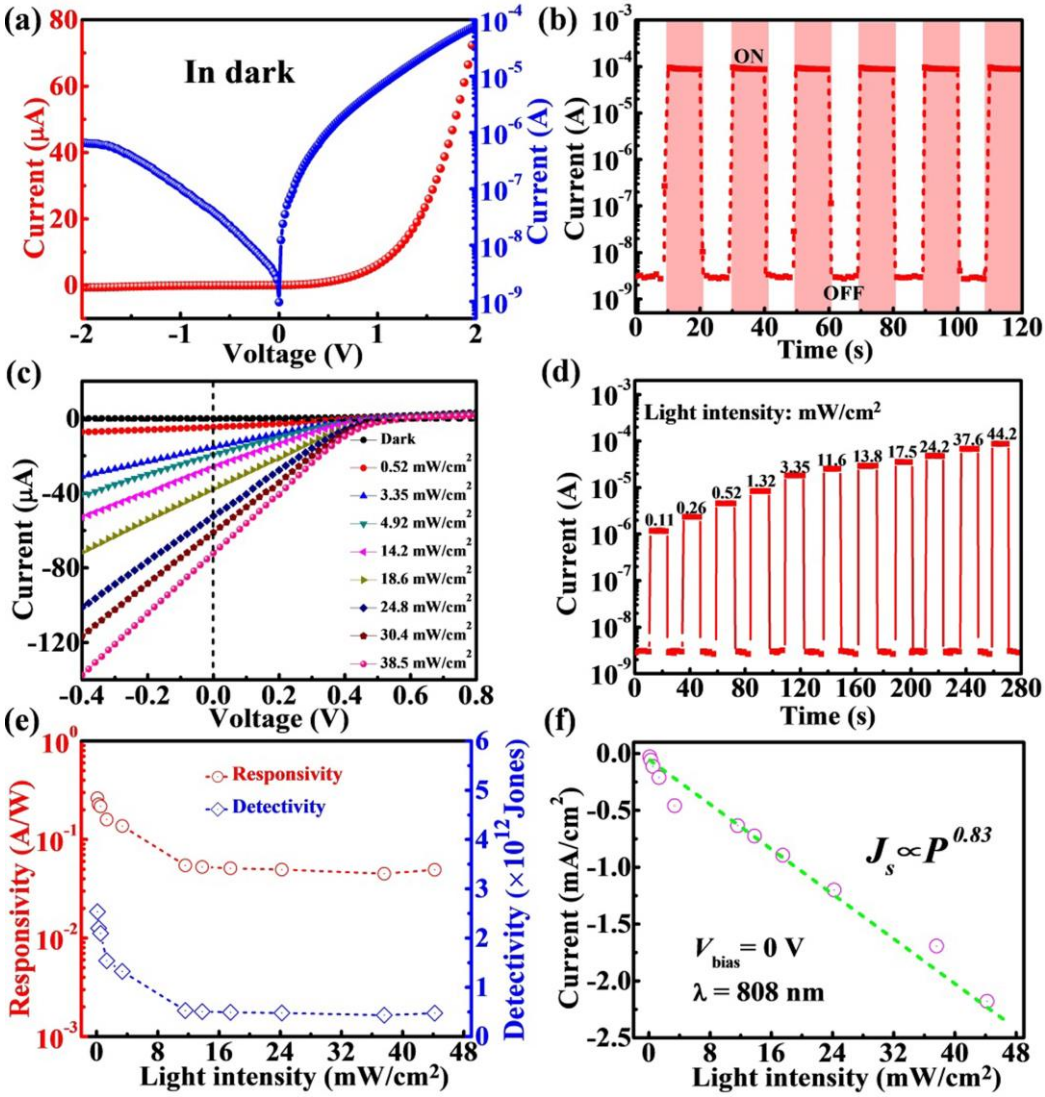

Figure 3 (a) The *I-V* curves of the heterojunction measured under dark (b) Photoresponse of the device under 808 nm (44.2 mW/cm^2) light illumination at zero bias. (c) *I-V* curves of the device at varied light intensity illustration (808 nm). (d) Photoresponse of the photodetector under various light intensity at 0 V. (e) Both responsivity and specific detectivity of the $PtSe_2$/GaAs heterojunction under 808 nm light illumination with different intensities. (f) Photocurrent density as a function of the incident-light intensity at zero bias.

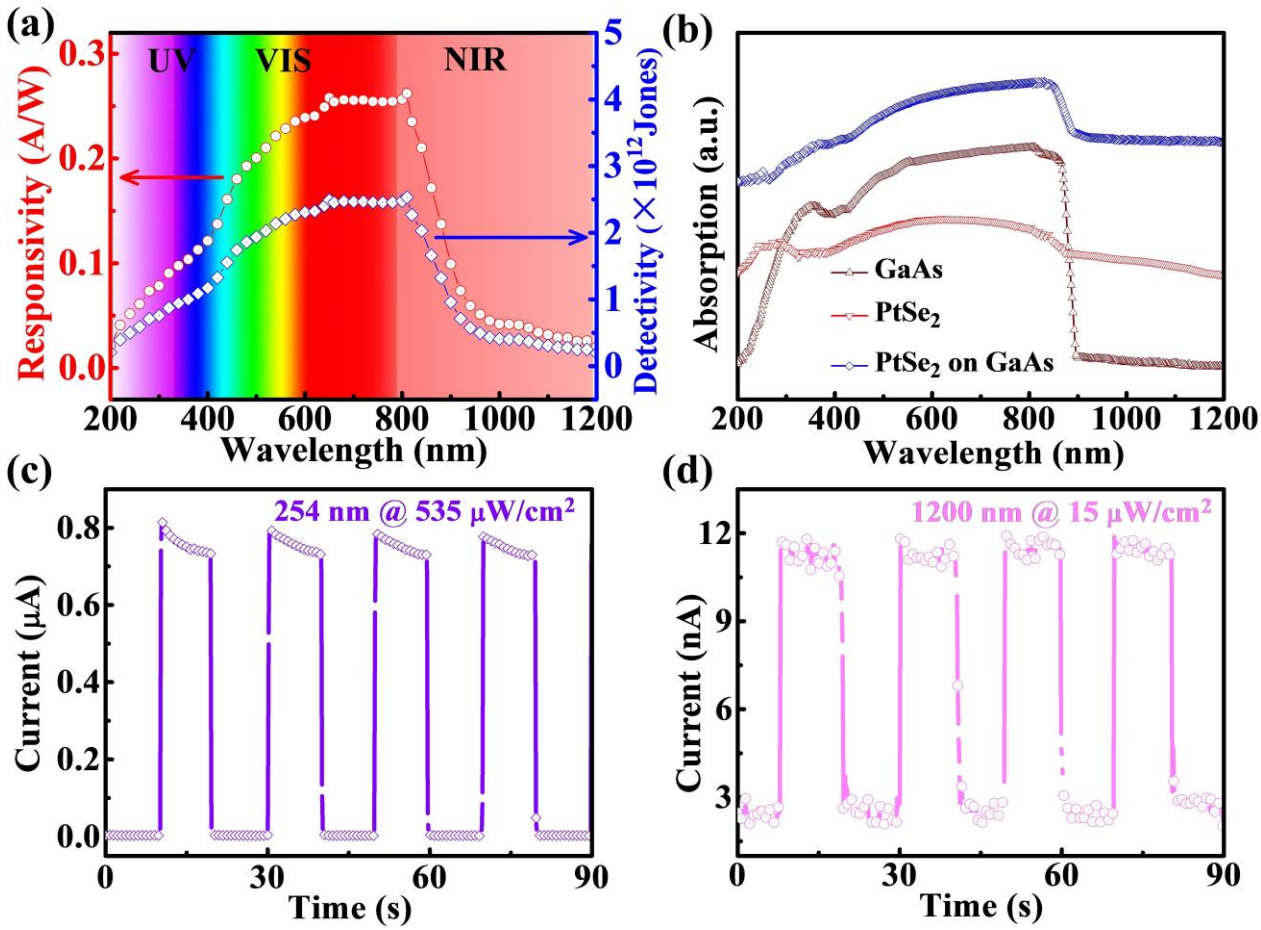

Figure 4 (a) Wavelength-dependent responsivity and specific detectivity of $PtSe_2$/GaAs (b) Absorption spectrum of the $PtSe_2$ film on GaAs substrate. The absorption spectra of $PtSe_2$ grown on quartz substrate under same conditions and bare substrate were also plotted for comparison. Time-dependent photoresponse of $PtSe_2$/GaAs hetrojunction excited by pulsed light at 254 nm (c) and 1200 nm (d) under zero bias condition.

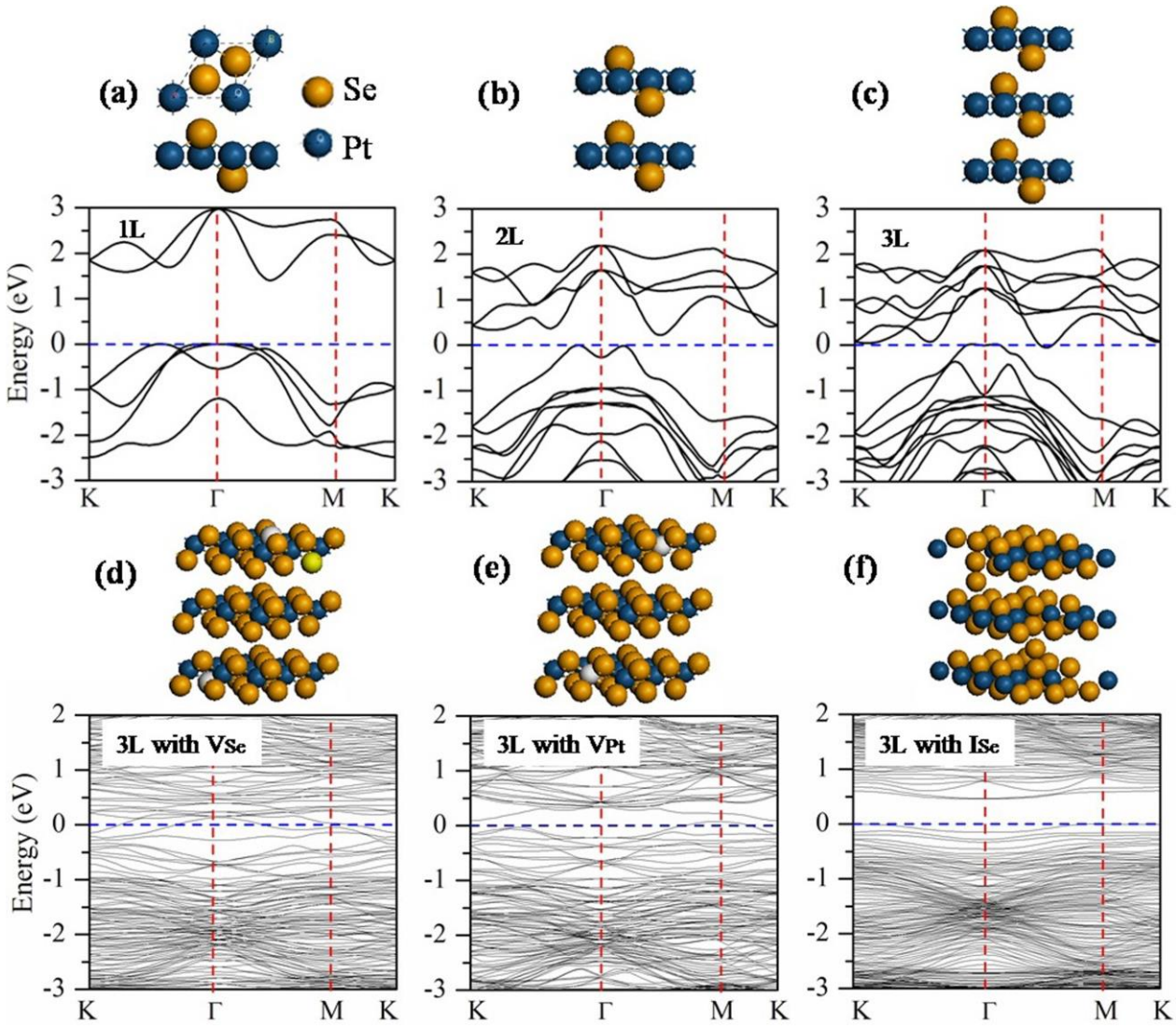

Figure 5 Geometrical and electronic band structures of the $PtSe_2$ primitive cells with (a) 1-layer (b) 2-layer, (c) 3-layer, and the 3×3 supercells with (d) Se-vacancy, (e) Pt-vacancy, and (f) interstitial incorporation of Se. The vacant atoms of Se and Pt are denoted by the white balls in (d) and (e). The Fermi level is located at 0 eV.

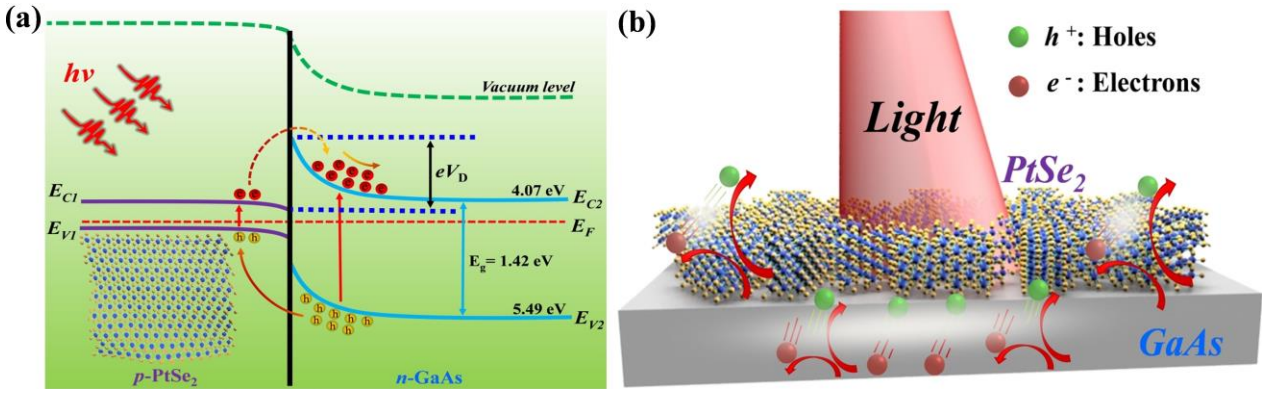

Figure 6 (a) The energy band diagram of the $PtSe_2$/GaAs heterojunction at zero bias under illumination. (b) Schematic illustration describing the rapid separation and movement of photo-excited carriers under illumination.

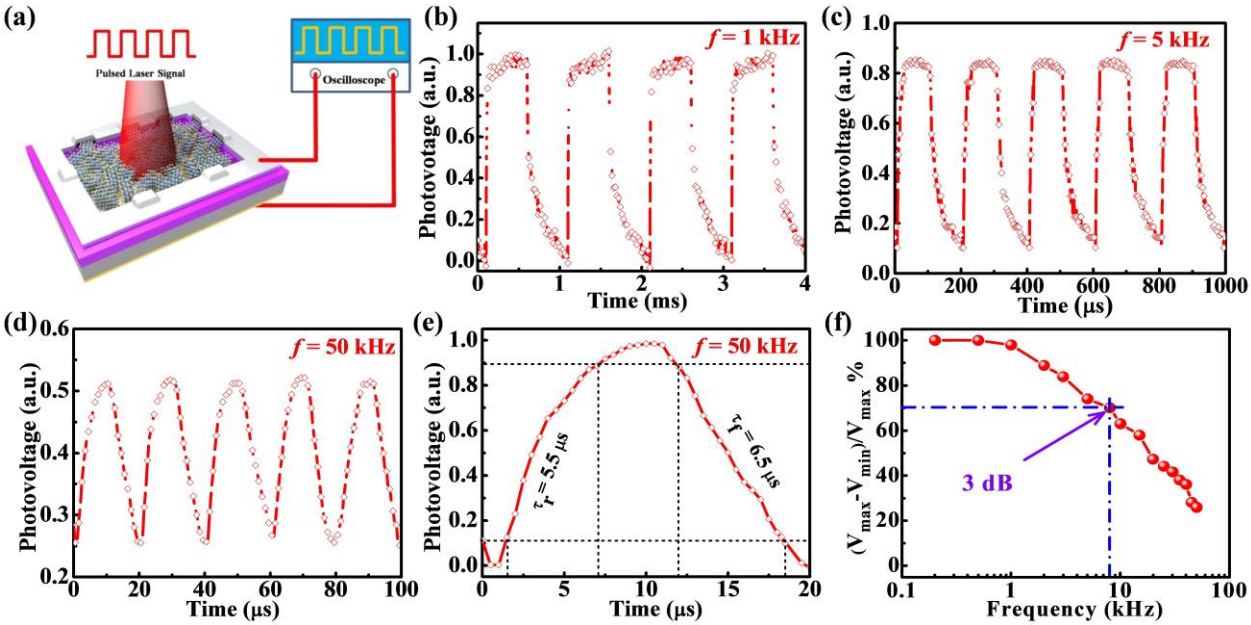

Figure 7 (a) The schematic illustration of the setup for studying the time response of the photodetector. Photoresponse of the self-driven $PtSe_2$/GaAs heterojunction photodetector to pulsed light irradiation (808 nm) with a frequency of (b) 1 kHz, (c) 5 kHz and (d) 50 kHz, respectively. (e) A single normalized cycle measured at 50 kHz for estimating both response time (τ_r) and recovery time (τ_f). (f) Relative balance (V_{max} - V_{min})/V_{max} versus switching frequency, showing the 3 dB cutoff frequency of ~8 kHz.

Table1. Comparison of characteristic parameters for 2D materials based photodetectors.

Device Structure	R	τ_r/τ_f	I_{light}/I_{dark}	D^* (Jone)	Measurement conditions	Spectral range	Ref
$PtSe_2$/GaAs heterojunction	262 mA/W	5.5/6.5 μs	~10^4	~10^{12}	V_{bi} = 0 V λ = 808 nm	Deep UV-NIR	This work
Few layer BP phototransistor	4.8 mA/W	1/4 ms	/	/	V_{ds}= 0.2 V Vg= 0 V λ = 640 nm	Visible-NIR	[3]
Graphene/GaAs nanocone array Schottky junction	1.73 mA/W	72/122 μs	~10^4	~10^{11}	V_{bi} = 0 V λ = 850 nm	Visible-NIR	[18]
Multilayer MoS_2 phototransistor	< 120 mA/W	/	/	~10^{10}	V_{ds} = 1 V V_g = 0 V λ = 633 nm	Visible-NIR	[38]
Graphene/β-Ga_2O_3 heterojunction	39.9 A/W	94.83/219.19 s	/	~10^{13}	V_{bi} = 2 V λ = 254 nm	Deep UV	[35]
WS_2/Si heterojunction	5.7 A/W	670/998 μs	~10^1	/	V_{bi} = -5 V λ = 660 nm	UV-NIR	[48]
MoS_2/Si heterojunction	11.9 A/W	30.5/71.6 μs	59.9	~10^{10}	V_{bi} = - 2 V λ = 650 nm	UV-NIR	[49]
Graphene/Si heterojunction	0.435 mA/W	1.2/3 ms	~10^4	~10^9	V_{bi} = 0 V λ = 850 nm	UV-NIR	[50]
Few layer WS_2 photosensor	0.092 mA/W	5.3/5.3 ms	/	/	V_{bi} = 5 V λ = 514 nm	Visible	[51]
Few layer InSe phototransistor	27 A/W	0.5/1.7 s	< 10	/	V_{ds}= 1 V V_g = 0 V λ = 370 nm	UV-NIR	[52]
Graphene/Ge heterojunction	51.8 mA/W	23/108 μs	~10^4	~10^{10}	V_{bi} = 0 V λ = 1550 nm	NIR	[53]

V_{bi} : The bias voltage; V_{ds} : Source-drain voltage; V_g : The positive gate voltage.

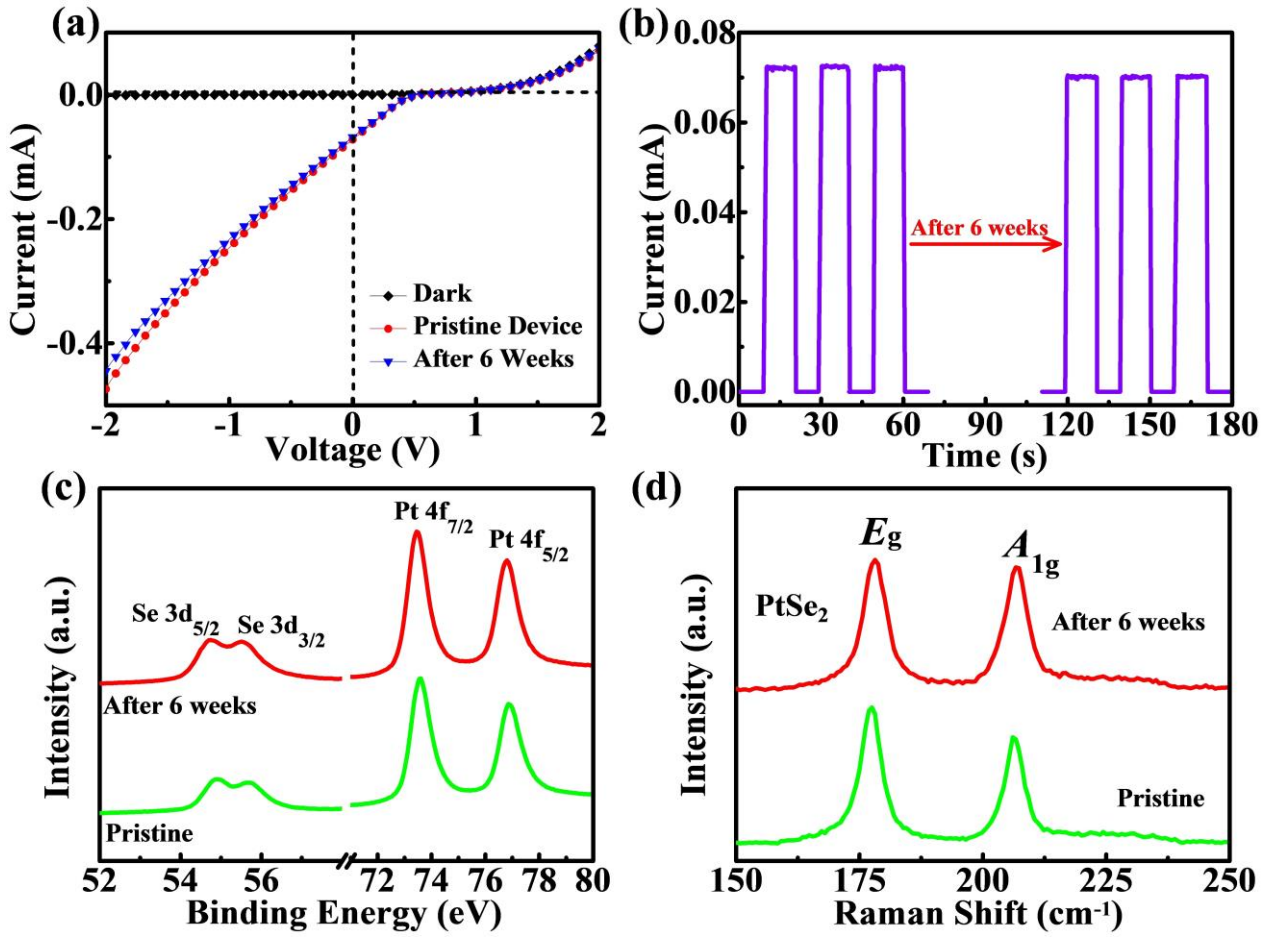

Figure 8 (a) The *I-V* characteristics and (b) zero-bias time-dependent photoresponse of the $PtSe_2$/GaAs photodetector after long-term storage. (c) Comparison of the XPS spectra of the $PtSe_2$ before and after 6 weeks. (d) Raman spectra of the $PtSe_2$ film before and after 6 weeks.

Table of Contents： This work shows the large-area growth of high quality vertically aligned $PtSe_2$, and its application to photodetector based on $PtSe_2$-GaAs heterojunction which exhibited a broadband sensitivity to illumination ranging from deep ultraviolet (DUV) to near infrared (NIR) light, with peak sensitivity in the region from 650 to 810 nm. The high-performance broadband photodetector will open up a new pathway for the development of next-generation 2D Group-10 materials based optoelectronic devices.